Progress In Electromagnetics Research C, Vol. 90, 195–208, 2019

Theoretical and Experimental Investigation of Ferrite-Loaded Waveguide for Ferrimagnetism Characterization

Hsin-Yu Yao, Wei-Chen Chang, Li-Wen Chang, and Tsun-Hsu Chang*

Abstract—This work proposes an approach to retrieve the ferrite's electromagnetic properties in a single compact configuration, simpler than the traditional measurement systems. The ferrite under test is fully inserted into a rectangular waveguide with a magnetic bias. The complex scattering parameters are theoretically analyzed under the consideration of modal effect at isotropy-anisotropy interfaces. Extraordinarily sharp Fano resonances are observed in the scattering spectrums, originating from the multimode interference inside the magnetized ferrite. There is good agreement among theoretical, experimental, and full-wave simulation results. This model can be further utilized to simultaneously retrieve all ferrite properties, including permittivity (ε), saturation magnetization ($4\pi M_s$), and magnetic linewidth (ΔH) from the measured scattering parameters, facilitating the designs and applications of ferrite devices.

1. INTRODUCTION

Ferrite materials with DC (direct current) magnetic biases have been studied for decades due to their promising applications in microwave region, such as isolators [1–3], circulators [4–6], phase shifter [7, 8], and high-density magnetic recording media [9]. To design these devices, the permittivity and the gyrotropic permeability of magnetized ferrites, must be known in advance. The perturbation method is commonly used to measure permittivity (ε) [10]. The saturation magnetization ($4\pi M_s$) is usually tested using the magnetometer method [11]. The cavity method is adapted to characterize the ferrite's line width (ΔH) and gyromagnetic ratio [12, 13]. These methods are quite narrowband in nature. Besides, different parameters have to be obtained using different experimental setups. There is a pressing need to measure all the key parameters in a single compact configuration without sample destruction. Quasi-optical system can characterize the ferrite's properties over a broadband. It is constructed by two horns respectively connecting to a source and a detector [14–17]. However, the required sample sizes must be much larger than beam sizes (about several cm^2 for microwave) in order to minimize edge diffraction [14]. This causes a lot of difficulties not only in the sample preparation but also in the uniformity of applied bias, leading to significant errors in the retrieved results.

On the other hand, rectangular waveguides partially or fully loaded with materials under test are frequently adopted for permittivity [18] and permeability [19–26] characterizations. Two major advantages are addressed here. Firstly, since electromagnetic (EM) wave is well confined within waveguides, edge diffraction is absent and the required sample size is shrunk down to the waveguide dimensions. As a consequence, sample preparation is easier and the required areas of bias fields with sufficient uniformity can be greatly reduced [19–21]. Secondly, the scattering parameters could be explicitly measured by network analyzers with reliable calibrations [19–21]. This feature implies that more accurate data could be obtained as compared with the aforementioned quasi-optical systems [14–17], in which the impedance mismatching between horns and free space is difficult to calibrate.

Received 26 October 2018, Accepted 24 January 2019, Scheduled 4 March 2019
* Corresponding author: Tsun-Hun Chang (thschang@phys.nthu.edu.tw).
The authors are with the Department of Physics, National Tsing Hua University, Hsinchu 300, Taiwan, R.O.C.

Unfortunately, most of ferrite-loaded waveguide systems are difficult to analyze [26]. It significantly increases the difficulty in permittivity and permeability retrieval processes. To this end, a part of previous efforts focused on a configuration of vertical-slab ferrites partially inserted inside rectangular waveguides, biased in the direction perpendicular to waveguide width [20, 21]. The eigenmodes' properties and the corresponding scattering parameters have been studied in [20] and further employed for characterization in [21]. Nevertheless, as ferrite slabs were partially inserted, how to precisely locate their positions and how to exquisitely control magnetic-bias profiles become tough issues in real measurements. Alternative scheme was proposed in [22–25], in which a rectangular waveguide is fully loaded with a magnetized sample. This configuration is much easier to assemble with less error in sample's location and better control of bias field, superior to the partially loaded systems [20, 21]. In [22], waveguide system with a single bulk magnetized sample was investigated. Although a model based on waveguide eigenmode expansion (mode matching) has been developed to solve scattering parameters, it cannot treat the case with ferrite due to high chromatic complexity in susceptibility. On the other hand, Tsutsumi et al. studied the case with Yttrium Iron Garnet (YIG) ferrite film that was grown on a bulk substrate and then sealed by a waveguide [23, 24]. An analysis method based on Fourier expansion (plane-wave expansion) was proposed for mode matching at boundaries. However, since these plane waves (as basis set) are not the eigenmodes of rectangular waveguide, the solution can be obtained only approximately and this method is relatively inefficient for retrieval. Besides, such thin-film configuration inherently suffers from non-negligible uncertainties for ferrite characterization owing to the presence of additional substrate and the mere perturbation effect of ultra-thin sample under test.

In this work, we consider a bulk ferrite standing alone within a rectangular waveguide. A rigorous model is developed to analyze the scattering process at an air-ferrite interface and an air-ferrite-air system. Based on the ferrite permittivity and gyrotropic permeability, the behaviors of new TE_{0n} eigenmodes (including their dispersions, attenuations and field profiles) under the presence of magnetized ferrite are completely discussed. Multimode coupling at air-ferrite interface and multimode interference in air-ferrite-air system are then analyzed, which give a clear picture of how higher-order modes are excited and interfere with the fundamental mode. With this knowledge, an analytical expression of the measurable scattering parameters for air-ferrite-air system is derived. We validate this model by examining a commercially available bulk YIG ferrite fully inserted within a standard X-band waveguide (8.00 GHz–12.00 GHz) and biased with a DC magnetic field (1000 Oe). The scattering parameters are calculated, which show perfect agreement with the experimental results and the simulation obtained from the full-wave solver (High-Frequency Structure Simulator, HFSS). This work lays the groundworks for fast and compact ferrite characterization in the microwave region.

2. NEW $\mathrm{TE_M}$ EIGENMODE CHARACTERISTICS IN A MAGNETICED FERRITE-LOADED WAVEGUIDE

When a DC magnetic field ($H_{\mathrm{DC}}\hat{y}$) is applied on a ferrite, randomly oriented unpaired spins would be aligned to precess around the bias, forming a net magnetization parallel to the bias [26, 29]. The precession frequency (ω_0) is $\mu_0\gamma H_{\mathrm{DC}}$, where μ_0 is the vacuum permeability and γ represents the charge to mass ratio of electron. Once the bias is strong enough to align all dipoles, the increase of magnetization gets saturated, resulting in a saturation magnetization ($M_s\hat{y}$). Since an unsaturated ferrite material is typically lossy for microwave [26, 30], in the following all samples are assumed to be at saturated state.

As an EM wave propagates in a biased ferrite, its AC (alternating current) magnetic field ($\vec{H}_{\mathrm{AC}}$) would induce an additional magnetization ($\vec{M}_{\mathrm{AC}}$). We assume $|\vec{H}_{\mathrm{AC}}| \ll H_{\mathrm{DC}}$ to ensure a perturbation effect of AC field on the dipole precession motion forced by the DC field. Since the dipole precession breaks the isotropic spatial symmetry, the susceptibility ($\overleftrightarrow{\chi}$) that relates the additional magnetization ($\vec{M}_{\mathrm{AC}}$) to the AC magnetic field ($\vec{H}_{\mathrm{AC}}$) turns anisotropic [22–26, 30]. Such susceptibility implies an anisotropic permeability ($\overleftrightarrow{\mu}$) described by a second-rank tensor:

$$\overleftrightarrow{\mu} = \mu_0 \begin{bmatrix} \mu_r & 0 & i\kappa_r \\ 0 & 1 & 0 \\ -i\kappa_r & 0 & \mu_r \end{bmatrix}, \tag{1}$$

with

$$\mu_r = 1 + \frac{\omega_0\omega_m\left[\omega_0^2 - \omega^2\left(1-\alpha^2\right)\right] + i\,\alpha\omega_m\omega\left[\omega_0^2 + \omega^2\left(1+\alpha^2\right)\right]}{\left[\omega_0^2 - \omega^2\left(1+\alpha^2\right)\right]^2 + 4\omega_0^2\omega^2\alpha^2},$$
$$\kappa_r = \frac{\omega\omega_m\left[\omega_0^2 - \omega^2\left(1+\alpha^2\right)\right] + i\,2\alpha\omega_0\omega_m\omega^2}{\left[\omega_0^2 - \omega^2\left(1+\alpha^2\right)\right]^2 + 4\omega_0^2\omega^2\alpha^2},$$

where ω is the carrier frequency of EM wave, and $\omega_m \equiv \mu_0\gamma M_s$. The damping factor, $\alpha = \mu_0\gamma\Delta H/2\omega$, is determined by the susceptibility linewidth ΔH of magnetic resonance. Note that the permeability tensor shown in Eq. (1) is for the case biased in $\hat{y}$ direction.

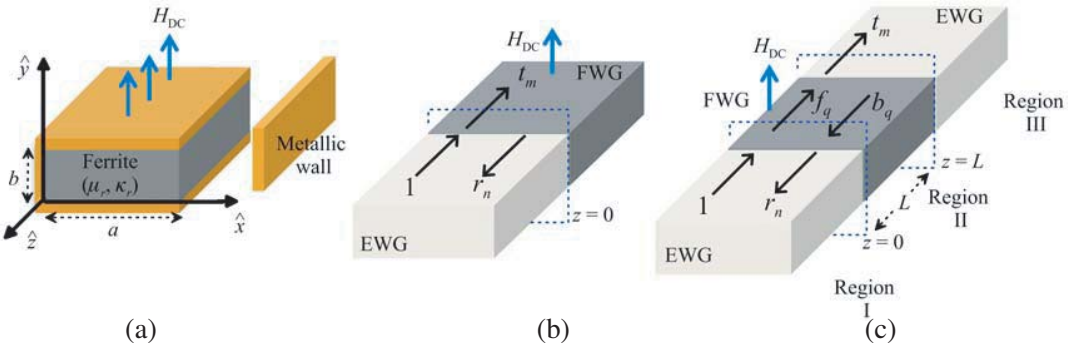

(a) (b) (c)

Figure 1. (a) Schematic diagram of a rectangular waveguide (with yellow metallic walls) fully loaded with a ferrite (gray region) biased in $\hat{y}$ direction ($H_{\rm DC}$). The waveguide width (height) is a (b). (b) An EM wave is incident from the empty waveguide (white region, denoted by EWG) to the waveguide filled with ferrite (gray region, denoted by FWG), passing through a single air-ferrite interface. (c) An EM wave passes through an air-ferrite-air system. A FWG (region II) is embedded between two EWGs at input (region I) and output (region III) sides. Note that the metallic walls in both (b) and (c) are not shown for clearness.

Figure 1(a) shows an infinitely-long rectangular waveguide fully filled by a ferrite with an external DC bias field ($H_{\rm DC}\hat{y}$). We consider only $\mathrm{TE}_{m0}^{\rm FWG}$ mode ("FWG" labels the quantities in the ferrite-loaded waveguide), whose $E_{z,m0}^{\rm FWG} = 0$ (TE mode) and all field components are invariant with respect to y ($\partial/\partial y = 0$). Substitute in Eq. (1) into Maxwell's equations, yielding

$$H_{x,m0}^{\rm FWG} = \frac{-1}{\omega\mu_e}\left(\beta_m^{\rm FWG}E_{y,m0}^{\rm FWG} + \frac{\kappa_r}{\mu_r}\frac{\partial E_{y,m0}^{\rm FWG}}{\partial x}\right), \tag{2}$$
$$H_{z,m0}^{\rm FWG} = \frac{-i}{\omega\mu_e}\left(\frac{\kappa_r}{\mu_r}\beta_m^{\rm FWG}E_{y,m0}^{\rm FWG} + \frac{\partial E_{y,m0}^{\rm FWG}}{\partial x}\right), \tag{3}$$
$$\left(\frac{\partial^2}{\partial x^2} + k_{T,m}^2\right)E_{y,m0}^{\rm FWG} = 0, \tag{4}$$

where $\mu_e \equiv \mu_0[(\mu_r^2 - \kappa_r^2)/\mu_r]$, $k_{T,m} = \sqrt{\mu_e\varepsilon\omega^2 - (\beta_m^{\rm FWG})^2}$, ε is the complex permittivity of ferrite, and $\beta_m^{\rm FWG}$ is the propagation constant. The other two field components ($E_{x,m0}^{\rm FWG}$ and $H_{y,m0}^{\rm FWG}$) are strictly zero. As shown in Eq. (4), $E_{y,m0}^{\rm FWG}$ satisfies the Helmholtz wave equation and serves as the generating function. The general solution of $E_{y,m0}^{\rm FWG}$ can be obtained by imposing the boundary conditions ($E_{y,m0}^{\rm FWG} = 0$ at $x = 0$ and $x = a$ due to metals), giving

$$E_{y,m0}^{\rm FWG} = \frac{i\omega\mu_0}{k_{T,m}}H_0\sin k_{T,m}x\; e^{i\beta_m^{\rm FWG}z}, \tag{5}$$

with $k_{T,m} = m\pi/a$, which is related to the geometrical cutoff frequency. Substituting Eq. (5) into Eqs. (2) and (3) gives

$$H_{x,m0}^{\mathrm{FWG}} = \frac{i\mu_0}{\mu_e} H_0 \left(-\frac{\beta_m^{\mathrm{FWG}}}{k_{T,m}} \sin k_{T,m}x - \frac{\kappa_r}{\mu_r} \cos k_{T,m}x \right) e^{i\beta_m^{\mathrm{FWG}} z}, \tag{6}$$

$$H_{z,m0}^{\mathrm{FWG}} = \frac{i\mu_0}{\mu_e} H_0 \left(\frac{\kappa_r}{\mu_r} \frac{\beta_m^{\mathrm{FWG}}}{k_{T,m}} \sin k_{T,m}x + \cos k_{T,m}x \right) e^{i\beta_m^{\mathrm{FWG}} z} \tag{7}$$

We note that the formulas of the transverse wave number ($k_{T,m}$), $\vec{E}_{m0}^{\mathrm{FWG}}$ field ($\vec{E}_{m0}^{\mathrm{FWG}} = E_{y,m0}^{\mathrm{FWG}}\hat{y}$), and $\vec{B}_{m0}^{\mathrm{FWG}}$ field ($\vec{B}_{m0}^{\mathrm{FWG}} = \vec{\vec{\mu}} \cdot \vec{H}_{m0}^{\mathrm{FWG}}$) are identical to their isotropic counterparts: $\mathrm{TE}_{m0}^{\mathrm{EWG}}$ mode in the empty waveguide ("EWG" labels the quantities in the empty waveguide) [26]. However, $\vec{H}_{m0}^{\mathrm{FWG}}$ field ($H_{x,m0}^{\mathrm{FWG}}\hat{x} + H_{z,m0}^{\mathrm{FWG}}\hat{z}$) obviously deviates from its isotropic counterpart ($\vec{H}_{m0}^{\mathrm{EWG}} = H_{x,m0}^{\mathrm{EWG}}\hat{x} + H_{z,m0}^{\mathrm{EWG}}\hat{z}$) owing to the anisotropic permeability tensor. The propagation constant of $\mathrm{TE}_{m0}^{\mathrm{FWG}}$ is

$$\beta_m^{\mathrm{FWG}} = \sqrt{\mu_e \varepsilon \omega^2 - k_{T,m}^2} = \sqrt{\mu_e \varepsilon \omega^2 - \left(\frac{m\pi}{a}\right)^2}, \tag{8}$$

which is determined by the effective permeability $\mu_e = \mu_0(\mu_r^2 - \kappa_r^2)/\mu_r$ rather than μ_r or κ_r.

In the following, a commercially available ferrite [Pacific Ceramics, Inc. (product #: 39-1780B)] with relative permittivity $(\varepsilon/\varepsilon_0) = 14.9$, loss tangent $(\tan\delta) = 10^{-4}$, saturation magnetization $(4\pi M_s) = 1780$ gauss, and linewidth $(\Delta H) = 25$ Oe, is chosen to demonstrate the ferrimagnetism and the corresponding dispersion of fundamental mode ($\mathrm{TE}_{10}^{\mathrm{FWG}}$). The DC magnetic bias field (H_{DC}) is 1000 Oe, implying a precession frequency $(\omega_0/2\pi)$ of 2.80 GHz. Figs. 2(a) and 2(b) demonstrate the frequency responses of μ_r (diagonal) and κ_r (off-diagonal), respectively. Both $\mathrm{Re}[\mu_r]$ and $\mathrm{Re}[\kappa_r]$ show gyromagnetic resonances at 2.80 GHz, matching the dipole precession frequency. On the other hand, the magnetic losses manifested in $\mathrm{Im}[\mu_r]$ and $\mathrm{Im}[\kappa_r]$ rapidly increase at the resonance and gradually decrease

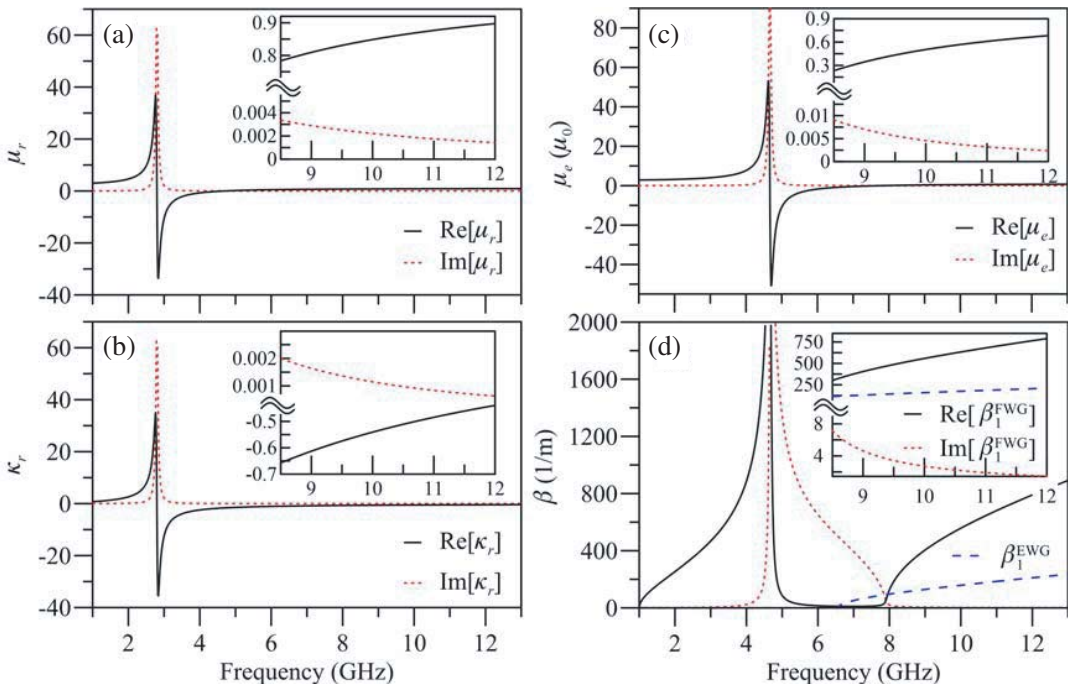

Figure 2. Ferrimagnetism of the biased YIG ferrite versus frequency. (a) μ_r, (b) κ_r, (c) μ_e, and (d) β_1^{FWG}. For all figures, the black solid (red dashed) curves represent the real (imaginary) parts. The blue dashed curve in (d) is the pure real propagation β_1^{EWG} of $\mathrm{TE}_{10}^{\mathrm{EWG}}$ mode in the empty X-band waveguide.

to their half maximums at 2.76 GHz and 2.83 GHz, implying a narrow magnetic resonant bandwidth of 0.07 GHz ($\Delta\omega/2\pi \approx \mu_0\gamma\Delta H$). The effective permeability (μ_e) that truly governs wave propagation in the biased ferrite is demonstrated in Fig. 2(c). We observe a strong blue shift of resonance from 2.80 GHz ($\omega_0/2\pi$) to 4.66 GHz [$\sqrt{\omega_0(\omega_0+\omega_m)}/2\pi$], because not only μ_r but also κ_r would jointly modulate the eigenmode characteristics.

Figure 2(d) demonstrates the propagation constant (β_1^{FWG}) of fundamental $\mathrm{TE}_{10}^{\mathrm{FWG}}$ mode in the ferrite-loaded X-band rectangular waveguide. The width (a) and the height (b) of X-band waveguide are 22.86 mm and 10.16 mm, respectively. The dispersion of $\mathrm{TE}_{10}^{\mathrm{EWG}}$ in the empty X-band waveguide (β_1^{EWG}) is delineated in Fig. 2(d) by the blue dashed curve. Strong resonance in β_1^{FWG} is observed near 4.66 GHz, analogous to the behavior of μ_e [Fig. 2(c)]. Below this resonant frequency, $\mathrm{Re}[\beta_1^{\mathrm{FWG}}]$ rapidly increases as frequency increases (with positive slope), revealing normal dispersion and slow-light effect. When the frequency increases across 4.66 GHz, $\mathrm{Re}[\beta_1^{\mathrm{FWG}}]$ decreases until 6.98 GHz, corresponding to anomalous dispersion and fast-light effect. From 4.66 GHz to 6.98 GHz, $\mathrm{Im}[\beta_1^{\mathrm{FWG}}]$ is several orders of magnitude larger than that in the normal-dispersion region, implying very strong attenuation. Such high attenuation majorly attributes to two loss mechanisms. Around 4.66 GHz, loss is dominated by magnetic-resonance absorption. Since both $|\mathrm{Re}[\mu_e]|$ and $|\mathrm{Im}[\mu_e]|$ are large, strong magnetic loss guarantees $\mathrm{Re}[\beta_1^{\mathrm{FWG}}] \neq 0$ [Eq. (8)]. This indicates that the mode could still propagate and meanwhile is quickly dissipated due to the resonant absorption.

As the operating frequency goes slightly beyond the resonant frequency (5.00 GHz–7.90 GHz), $\mathrm{Re}[\mu_e]$ is negative and shows a magnitude much greater than $|\mathrm{Im}[\mu_e]|$, suggesting the disappearance of magnetic resonance. However, the large negative $\mathrm{Re}[\mu_e]$ with negligible $\mathrm{Im}[\mu_e]$ turns β_1^{FWG} into nearly pure imaginary {$\mathrm{Re}[\beta_1^{\mathrm{FWG}}] \approx 0$, Eq. (8)}, making the mode become evanescent (non-propagable). This results in an additional stopband from 5.00 GHz to 7.90 GHz. The loss mechanism for this range is consequently governed by return loss, which fundamentally differs from the absorption loss around 4.66 GHz–5.00 GHz. When the operating band is far from the resonance and the stopband, for example from 8.50 GHz to 12.00 GHz, $\mathrm{TE}_{10}^{\mathrm{FWG}}$ mode becomes propagable with relatively weak attenuation {$\mathrm{Re}[\beta_1^{\mathrm{FWG}}] \gg \mathrm{Im}[\beta_1^{\mathrm{FWG}}]$, the inset of Fig. 2(d)}, showing normal dispersion. It is important to emphasize that the anomalous dispersion with high attenuation at 4.66 GHz–7.90 GHz would significantly reduce the strength of transmitting signal from the ferrite. This feature is useful for the applications in broadband filters or switches [23–25], however, such high loss would seriously increase the difficulty in measurement for ferrite characterization owing to the sensitivity limitation. On the contrary, the two special features for far-resonance operation from 8.50 GHz to 12.00 GHz — the normal dispersion and the weak attenuation, make this band more suitable for measurement. The following analyses will therefore focus on 8.50 GHz–12.00 GHz (X-band region).

The transverse magnetic fields of $\mathrm{TE}_{10}^{\mathrm{FWG}}$ forward (backward) wave [denoted as $H_{x,10}^{\mathrm{FWG},+}(H_{x,10}^{\mathrm{FWG},-})$] are demonstrated in Fig. 3 by the black solid curves (red solid curves). Four representative frequencies at 8.50 GHz [Fig. 3(a)], 9.50 GHz [Fig. 3(b)], 10.50 GHz [Fig. 3(c)], and 11.50 GHz [Fig. 3(d)] are selected for demonstration. The counterparts in the empty waveguide are illustrated by the blue dashed curves ($\mathrm{TE}_{10}^{\mathrm{EWG},+}$ forward wave, $H_{x,10}^{\mathrm{EWG},+}$) and the green dashed curves ($\mathrm{TE}_{10}^{\mathrm{EWG},-}$ backward wave, $H_{x,10}^{\mathrm{EWG},-}$) for comparison. Notice that the transverse electric fields in the presence ($E_{y,10}^{\mathrm{FWG}}$) and the absence of the magnetized ferrite ($E_{y,10}^{\mathrm{EWG}}$) are unchanged so that they are not shown here. A few observations of Fig. 3 can be made: firstly, both $H_{x,10}^{\mathrm{FWG},+}$ and $H_{x,10}^{\mathrm{FWG},-}$ in the ferrite-loaded waveguide are frequency dependent, because μ_r and κ_r are highly dispersive. Secondly, both $H_{x,10}^{\mathrm{FWG},+}$ and $H_{x,10}^{\mathrm{FWG},-}$ would not become zero at the waveguide boundaries ($x = 0$ and $x = a$), whereas those in the empty waveguide ($H_{x,10}^{\mathrm{EWG},+}$ and $H_{x,10}^{\mathrm{EWG},-}$) would. Although $H_{x,10}^{\mathrm{FWG}} \neq 0$ at $x = 0$ and $x = a$, $B_{x,10}^{\mathrm{FWG}}[\propto (\mu_r H_{x,10}^{\mathrm{FWG}} + i\kappa_r H_{z,10}^{\mathrm{FWG}})]$ is zero on all metal walls. Thirdly, $H_{x,10}^{\mathrm{FWG},+}$ ($H_{x,10}^{\mathrm{FWG},-}$) significantly differs from $H_{x,10}^{\mathrm{EWG},+}$ ($H_{x,10}^{\mathrm{EWG},-}$) for near-resonance operation ($\sim$ 8.50 GHz), while they are close to each other for far-resonance operation ($\sim$ 11.50 GHz). The deviation between $H_{x,10}^{\mathrm{FWG}}$ and $H_{x,10}^{\mathrm{EWG}}$ results from the anisotropism, which is manifested by how far μ_r and κ_r deviate from 1 and 0, respectively (Fig. 2). Finally, although the forward and backward waves in the ferrite-loaded waveguide share the

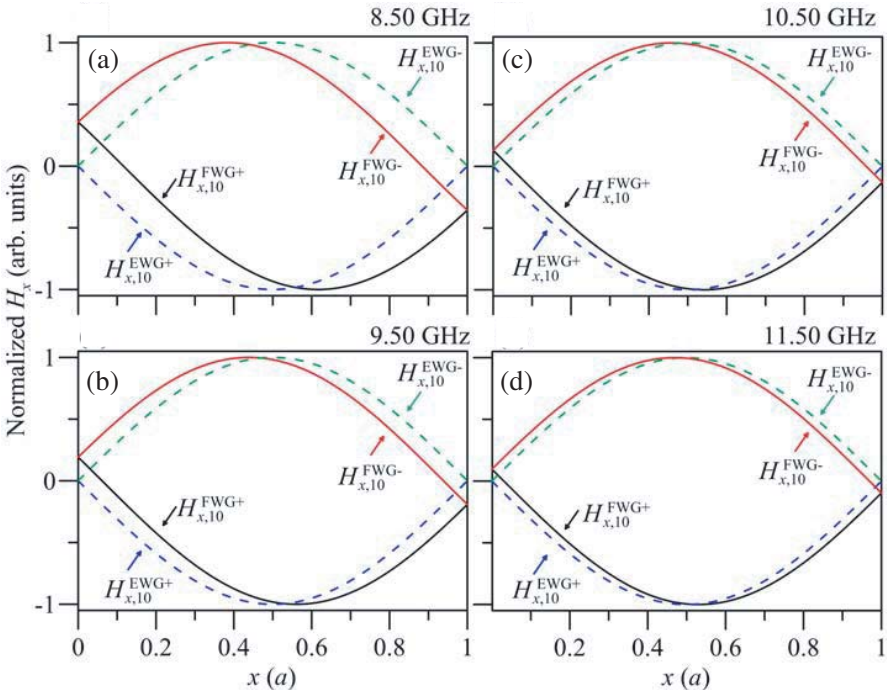

Figure 3. Normalized magnetic fields of $\mathrm{TE}_{10}^{\mathrm{FWG}}$ mode ($H_{x,10}^{\mathrm{FWG}}$) and $\mathrm{TE}_{10}^{\mathrm{EWG}}$ mode ($H_{x,10}^{\mathrm{EWG}}$). For forward wave (denoted by "+" sign in superscript), $H_{x,10}^{\mathrm{FWG},+}$ ($H_{x,10}^{\mathrm{EWG},+}$) is shown by the black solid curve (blue dashed curve), while for backward wave (denoted by "−" sign in superscript), $H_{x,10}^{\mathrm{FWG},-}$ ($H_{x,10}^{\mathrm{EWG},-}$) is shown by the red solid curve (green dashed curve). (a) At 8.50 GHz. (b) At 9.50 GHz. (c) At 10.50 GHz. (d) At 11.50 GHz.

same propagation constant ($|\beta_1^{\mathrm{FWG}}|$), their magnetic fields ($H_{x,10}^{\mathrm{FWG},+}$ and $H_{x,10}^{\mathrm{FWG},-}$) show antisymmetric spatial distributions in x with a 180° phase difference. This feature implies the forward energy flux ($\propto \mathrm{Re}[E_{y,10}^{\mathrm{FWG}} H_{x,10}^{\mathrm{FWG},+*}]$) and the backward energy flux ($\propto \mathrm{Re}[E_{y,10}^{\mathrm{FWG}} H_{x,10}^{\mathrm{FWG},-*}]$) transport the energy at different spatial channels in the ferrite-loaded waveguide.

3. MODAL ANALYSIS FOR A SINGLE AIR-FERRITE INTERFACE

In this section, the scattering behaviors of a fundamental $\mathrm{TE}_{10}^{\mathrm{EWG}}$ mode at an air-ferrite interface (incident from the empty waveguide) are studied [Fig. 1(b)]. Multiple modes with the same symmetry as the incoming $\mathrm{TE}_{10}^{\mathrm{EWG}}$ mode, on both sides of the interface, will be excited in order to meet boundary conditions. It is so-called the modal effect [20–28]. In the ferrite-loaded waveguide multiple $\mathrm{TE}_{m0}^{\mathrm{FWG}}$ modes will be excited as the transmitted wave, whereas the reflected wave at the empty waveguide is composed of multiple $\mathrm{TE}_{n0}^{\mathrm{EWG}}$ modes. The boundary conditions at the interface ($z = 0$) require

$$E_{y,10}^{\mathrm{EWG}} + \sum_{n=1}^{\infty} E_{y,n0}^{\mathrm{EWG}}\, r_n = \sum_{m=1}^{\infty} E_{y,m0}^{\mathrm{FWG}}\, t_m, \tag{9}$$

$$H_{x,10}^{\mathrm{EWG}} - \sum_{n=1}^{\infty} H_{x,n0}^{\mathrm{EWG}}\, r_n = \sum_{m=1}^{\infty} H_{x,m0}^{\mathrm{FWG}}\, t_m, \tag{10}$$

where t_m is the field transmission coefficient of $\mathrm{TE}_{m0}^{\mathrm{FWG}}$ and r_n is the field reflection coefficient of $\mathrm{TE}_{n0}^{\mathrm{EWG}}$. Substituting the eigenmode electric and magnetic fields {$E_{y,m0}^{\mathrm{FWG}}$ in Eq. (5), $H_{x,m0}^{\mathrm{FWG}}$ in Eq. (6), and $E_{y,n0}^{\mathrm{EWG}}$

$(H_{x,n0}^{\mathrm{EWG}})$ in [26]} into Eqs. (9) and (10) gives

$$\sin\frac{\pi x}{a}+\sum_{n=1}^{\infty}\frac{1}{n}\sin\frac{n\pi x}{a}\,r_n\;=\;\sum_{m=1}^{\infty}\frac{1}{m}\sin\frac{m\pi x}{a}\,t_m, \tag{11}$$

$$\beta_1^{\mathrm{EWG}}\sin\frac{\pi x}{a}-\sum_{n=1}^{\infty}\frac{\beta_n^{\mathrm{EWG}}}{n}\sin\frac{n\pi x}{a}\,r_n\;=\;\frac{\mu_0}{\mu_e}\sum_{m=1}^{\infty}\left(\frac{\beta_m^{\mathrm{FWG}}}{m}\sin\frac{m\pi x}{a}+\frac{\kappa_r}{\mu_r}\frac{\pi}{a}\cos\frac{m\pi x}{a}\right)\,t_m. \tag{12}$$

Multiplying Eq. (11) by $\sin(p\pi x/a)$, integrating from $x = 0$ to a, and using the trigonometric orthogonality yields

$$\delta_{p1}+r_p\;=t_p, \tag{13}$$

where δ represents the Kronecker delta symbol. Applying the same calculation to Eq. (12) gives

$$\beta_1^{\mathrm{EWG}}\delta_{p1}-\beta_p^{\mathrm{EWG}}r_p=\frac{\mu_0}{\mu_e}\left(\beta_p^{\mathrm{FWG}}t_p+\frac{\kappa_r}{\mu_r}\frac{2}{a}\sum_{m=1}^{\infty}I_{pm}\,t_m\right), \tag{14}$$

in which $I_{pm} = [p^2/(p^2 - m^2)](1 - \cos p\pi\ \cos m\pi)$. For numerical calculation we must truncate the summation in Eq. (14) to N, i.e., the total number of eigenmodes considered in the expansion. In the present analysis, the total numbers of modes considered at both sides of interface are assumed equal. In principle, the larger the N is, the more accurate the result is at the expense of long computation time. Substituting r_p from Eq. (13) into Eq. (14) gives a set of equations for solving t_m

$$\sum_{m=1}^{N}M_{pm}\,t_m=2\beta_1^{\mathrm{EWG}}\delta_{p1}, \tag{15}$$

where M_{pm} is

$$M_{pm}=\left(\frac{\mu_0}{\mu_e}\beta_p^{\mathrm{FWG}}+\beta_p^{\mathrm{EWG}}\right)\delta_{pm}+\frac{\mu_0}{\mu_e}\frac{\kappa_r}{\mu_r}\frac{2}{a}I_{pm}.$$

Based on t_m and r_n, the transmittance (T_m) and reflectance (R_n) can be calculated from Poynting vectors as $T_m = \mathrm{Re}[(\beta_m^{\mathrm{FWG}*}\,\mu_0)/(\beta_1^{\mathrm{EWG}}\mu_e^* m^2)] \times |t_m|^2$ and $R_n = \mathrm{Re}[(\beta_n^{\mathrm{EWG}*})/(\beta_1^{\mathrm{EWG}} n^2)] \times |r_n|^2$, respectively.

In what follows, the modal effect at an air-ferrite interface is analyzed with $N = 20$, which is found to be sufficient for converged results. The bias and the ferrite characteristics are identical to those selected in Sec. 2. Fig. 4(a) shows $|t_m|$ of the first eight $\mathrm{TE}_{m0}^{\mathrm{FWG}}$ modes $(1 \le m \le 8)$ in the ferrite-loaded waveguide, while Fig. 5(b) demonstrates $|r_n|$ of the first eight $\mathrm{TE}_{n0}^{\mathrm{EWG}}$ modes $(1 \le n \le 8)$ in the empty

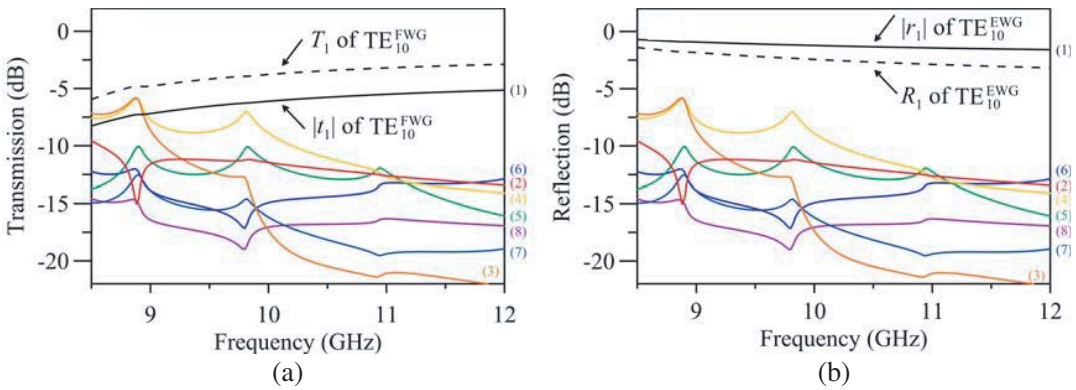

Figure 4. (a) $|t_m|$ of the first eight excited $\mathrm{TE}_{m0}^{\mathrm{FWG}}$ modes $(1 \le m \le 8$, the solid curves) at the ferrite-loaded side Transmittance T_1 of $\mathrm{TE}_{10}^{\mathrm{FWG}}$ mode is shown in the dashed curve. (b) $|r_n|$ of the first eight excited $\mathrm{TE}_{n0}^{\mathrm{EWG}}$ modes $(1 \le n \le 8$, the solid curves) at the empty side Reflectance R_1 of $\mathrm{TE}_{10}^{\mathrm{EWG}}$ mode (the only propagating mode) is shown in the dashed curve.

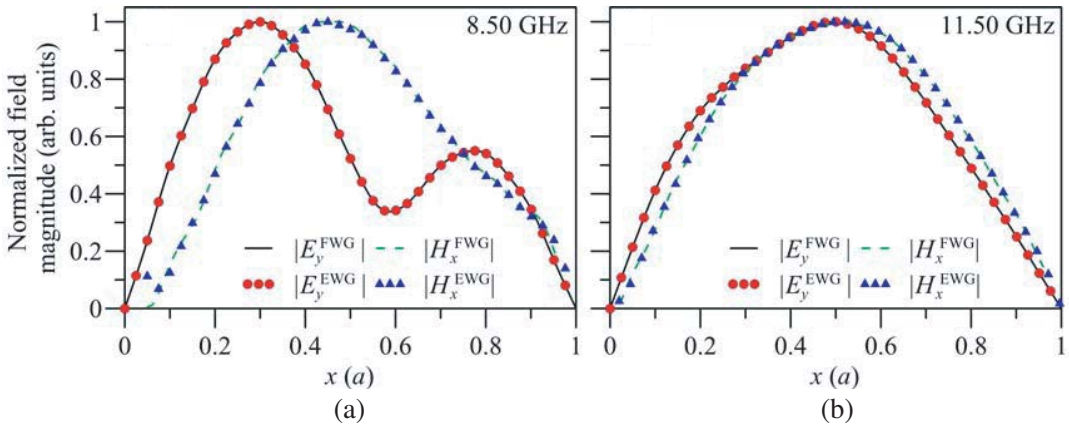

Figure 5. Normalized transverse electric and magnetic field profiles at the both sides of air-ferrite interface. (a) At 8.50 GHz for near-resonance operation. (b) At 11.50 for far-resonance operation. Color codes: black solid ($|E_y^{\mathrm{FWG}}|$), green dashed ($|H_x^{\mathrm{FWG}}|$), red dots ($|E_y^{\mathrm{EWG}}|$), and blue triangles ($|H_x^{\mathrm{EWG}}|$).

waveguide. Notably, $|t_m|$ with $9 \leq m \leq 20$ and $|r_n|$ with $9 \leq n \leq 20$ are all smaller than -20 dB and thus are not shown for clarity.

Comparing Figs. 4(a) and 4(b), we find that if $m = n \neq 1$, $|r_n|$ is equal to $|t_m|$. As explained, $\mathrm{TE}_{n0}^{\mathrm{EWG}}$ and $\mathrm{TE}_{m0}^{\mathrm{FWG}}$ possess the identical transverse electric field ($E_{y,n0}^{\mathrm{EWG}} = E_{y,m0}^{\mathrm{FWG}}$) as long as their mode orders are equal ($m = n$). Since the superposed transverse electric field must continue, the more the higher-order $\mathrm{TE}_{n0}^{\mathrm{EWG}}$ mode is excited at the empty side, the more the $\mathrm{TE}_{m0}^{\mathrm{FWG}}$ mode ($m = n > 1$) will be correspondingly coupled out at the ferrite-loaded side. However, $|t_1|$ and $|r_1|$ are not necessarily so due to the involvement of the incident wave. Three waves — the incident $\mathrm{TE}_{10}^{\mathrm{EWG}}$, the reflected $\mathrm{TE}_{10}^{\mathrm{EWG}}$, and the transmitted $\mathrm{TE}_{10}^{\mathrm{FWG}}$ work together to ensure the continuity of transverse electric field.

As demonstrated in Fig. 3, the magnetic field of $\mathrm{TE}_{10}^{\mathrm{FWG}}$ mode ($H_{x,10}^{\mathrm{FWG}}$) differs from that of the incoming $\mathrm{TE}_{10}^{\mathrm{EWG}}$ mode ($H_{x,10}^{\mathrm{EWG}}$), especially for relatively near-resonance operation [e.g., 8.50 GHz to 9.00 GHz, Fig. 3(a)]. Therefore, considerable higher-order modes in the ferrite-loaded waveguide must be excited together with the fundamental $\mathrm{TE}_{10}^{\mathrm{FWG}}$ mode to meet the continuity of transverse magnetic field. It can be seen that $|t_3| = -7.15$ dB and $|t_4| = -7.57$ dB at 8.50 GHz, both of which are greater than $|t_1|$ (-8.27 dB). This indicates that $\mathrm{TE}_{30}^{\mathrm{FWG}}$ and $\mathrm{TE}_{40}^{\mathrm{FWG}}$ modes dominate the modal coupling rather than $\mathrm{TE}_{10}^{\mathrm{FWG}}$ mode. On the contrary, $H_{x,10}^{\mathrm{FWG}}$ strongly resembles $H_{x,10}^{\mathrm{EWG}}$ for far-resonance operation [e.g., 10.00 GHz to 12.00 GHz, Fig. 3(d)]. As $H_{x,10}^{\mathrm{EWG}}$ highly overlaps with $H_{x,10}^{\mathrm{FWG}}$ rather than any other $H_{x,m0}^{\mathrm{FWG}}$ with $m > 1$, only the fundamental $\mathrm{TE}_{10}^{\mathrm{FWG}}$ mode dominates the coupling ($|t_1| = -5.30$ dB) and all higher-order $\mathrm{TE}_{m0}^{\mathrm{FWG}}$ modes are strongly suppressed to below -10 dB.

The transmittance of $\mathrm{TE}_{10}^{\mathrm{FWG}}$ mode (T_1) and the reflectance of $\mathrm{TE}_{10}^{\mathrm{EWG}}$ mode (R_1) are illustrated by the dashed curves in Figs. 4(a) and 4(b), respectively. Although higher-order $\mathrm{TE}_{m0}^{\mathrm{FWG}}$ and $\mathrm{TE}_{n0}^{\mathrm{EWG}}$ modes will be excited most of them (except $\mathrm{TE}_{20}^{\mathrm{FWG}}$) are evanescent and hence cannot carry power due to below-cutoff operation. Thus, T_m with $m \geq 2$ and R_n with $n \geq 2$ are all below -20 dB, not shown for clearness. Note that the total transmission power ($\sim T_1 < -3$ dB) is less than the total reflected power ($R_1 > -3$ dB) for the whole X band. The high reflection mainly results from the large permittivity of ferrite which leads to serious impedance mismatching between $\mathrm{TE}_{10}^{\mathrm{FWG}}$ mode and $\mathrm{TE}_{10}^{\mathrm{EWG}}$ mode.

Figures 5(a) and 5(b) show the profiles of superimposed transverse fields at 8.50 GHz (near-resonance operation) and 11.50 GHz (far-resonance operation), respectively. The superposed electric field $|E_y|$ at the ferrite-loaded (empty) side is illustrated by the black solid curve (red dots) and the superposed magnetic field $|H_x|$ at the ferrite-loaded (empty) side is illustrated by the green dashed curve (blue triangles). As expected, $|E_y|$ and $|H_x|$ are continuous at the air-ferrite interface, verifying the validity of the present theory.

4. MODAL ANALYSIS FOR AN AIR-FERRITE-AIR SYSTEM

In this section, we extend the modal analysis to study the scattering problem in an air-ferrite-air system [Fig. 1(c)], which is a more realistic configuration for ferrite characterization. When the incident $\mathrm{TE}_{10}^{\mathrm{EWG}}$ mode impinges on the air-to-ferrite interface ($z = 0$, B_1), it would be partially reflected and partially transmitted. When the injected signal (composed of multiple $\mathrm{TE}_{q0}^{\mathrm{FWG}}$ modes) propagates through the ferrite over a thickness L (region II) and reaches the ferrite-to-air interface ($z = L$, B_2), it would also be partially reflected and partially transmitted. The reflected part subsequently bounces back and forth between the two interfaces, forming a sequence of consecutive reflection echoes. In steady state, the total forward-wave field and backward-wave field inside the ferrite are built up. Similar to the analysis in Sec. 3, the continuities of E_y and H_x at $z = 0$ respectively require

$$\sin\frac{\pi x}{a}+\sum_{n=1}^{\infty}\frac{1}{n}\sin\frac{n\pi x}{a}\,r_n\,=\,\sum_{p=1}^{\infty}\frac{1}{p}\sin\frac{p\pi x}{a}\,\left(f_p+b_p\right), \tag{16}$$

$$\beta_1^{\mathrm{EWG}}\sin\frac{\pi x}{a}-\sum_{n=1}^{\infty}\frac{\beta_n^{\mathrm{EWG}}}{n}\sin\frac{n\pi x}{a}\,r_n\,=\,\frac{\mu_0}{\mu_e}\sum_{p=1}^{\infty}\left[\frac{\beta_p^{\mathrm{FWG}}}{p}\sin\frac{p\pi x}{a}\,(f_p-b_p)+\frac{\kappa_r}{\mu_r}\frac{\pi}{a}\cos\frac{p\pi x}{a}\,(f_p+b_p)\right], \tag{17}$$

and the continuities of E_y and H_x at $z = L$ respectively require

$$\sum_{p=1}^{\infty}\frac{1}{p}\sin\frac{p\pi x}{a}\left(e^{i\beta_p^{\mathrm{FWG}}L}\,f_p+e^{-i\beta_p^{\mathrm{FWG}}L}\,b_p\right)\,=\,\sum_{m=1}^{\infty}\frac{1}{m}\sin\frac{m\pi x}{a}e^{i\beta_m^{\mathrm{EWG}}L}\,t_m, \tag{18}$$

$$\frac{\mu_0}{\mu_e}\sum_{p=1}^{\infty}\left[\begin{array}{l}\dfrac{\beta_p^{\mathrm{FWG}}}{p}\sin\dfrac{p\pi x}{a}\left(e^{i\beta_p^{\mathrm{FWG}}L}\,f_p-e^{-i\beta_p^{\mathrm{FWG}}L}\,b_p\right)\\ +\dfrac{\kappa_r}{\mu_r}\dfrac{\pi}{a}\cos\dfrac{p\pi x}{a}\left(e^{i\beta_p^{\mathrm{FWG}}L}\,f_p+e^{-i\beta_p^{\mathrm{FWG}}L}\,b_p\right)\end{array}\right]\,=\,\sum_{m=1}^{\infty}\frac{\beta_m^{\mathrm{EWG}}}{m}\sin\frac{m\pi x}{a}e^{i\beta_m^{\mathrm{EWG}}L}\,t_m, \tag{19}$$

in which r_n, f_p, b_p, and t_m respectively represent the field reflection coefficient ($\mathrm{TE}_{n0}^{\mathrm{EWG}-}$ in region I), forward-wave coefficient ($\mathrm{TE}_{p0}^{\mathrm{FWG}+}$ in region II), backward-wave coefficient ($\mathrm{TE}_{p0}^{\mathrm{FWG}-}$ in region II), and field transmission coefficient ($\mathrm{TE}_{m0}^{\mathrm{EWG}+}$ in region III). Multiplying both Eqs. (16) and (18) by $\sin(q\pi x/a)$, integrating them from $x = 0$ to a and employing the trigonometric orthogonality for solving the forward-wave and backward-wave coefficients, we obtain

$$f_q\,=\,\frac{-e^{-i\beta_1^{\mathrm{FWG}}L}\delta_{q1}-e^{-i\beta_q^{\mathrm{FWG}}L}\,r_q+e^{i\beta_q^{\mathrm{EWG}}L}\,t_q}{2i\sin\beta_q^{\mathrm{FWG}}L}, \tag{20}$$

$$b_q\,=\,\frac{e^{i\beta_1^{\mathrm{FWG}}L}\delta_{q1}+e^{i\beta_q^{\mathrm{FWG}}L}\,r_q-e^{i\beta_q^{\mathrm{EWG}}L}\,t_q}{2i\sin\beta_q^{\mathrm{FWG}}L} \tag{21}$$

Substituting Eqs. (20) and (21) into Eqs. (17) and (19), and repeating the similar procedure to remove sine functions by trigonometric orthogonality, we can express r_n in terms of t_m

$$r_n=-\delta_{n1}+\sum_{m=1}^{N}\left[\left(-i\frac{\mu_e}{\mu_0}\frac{\beta_m^{\mathrm{EWG}}}{\beta_m^{\mathrm{FWG}}}\sin\beta_m^{\mathrm{FWG}}L+\cos\beta_m^{\mathrm{FWG}}L\right)\delta_{nm}+i\frac{\kappa_r}{\mu_r}\frac{2}{a}\frac{\sin\beta_n^{\mathrm{FWG}}L}{\beta_n^{\mathrm{FWG}}}I_{nm}\right]e^{i\beta_m^{\mathrm{EWG}}L}\,t_m \tag{22}$$

and get a set of equations for solving t_m:

$$\sum_{m=1}^{N}M_{qm}\,t_m=2\beta_1^{\mathrm{EWG}}\delta_{q1} \tag{23}$$

where M_{qm} could be decomposed into several sub-matrices ($M_{qm}\equiv X_q\delta_{qm}+Y_{qm}+Z_{qm}$) with

$$X_q\,=\,-i\frac{\mu_0}{\mu_e}\beta_q^{\mathrm{FWG}}\frac{e^{i\beta_q^{\mathrm{EWG}}L}}{\sin\beta_q^{\mathrm{FWG}}L}+2\beta_q^{\mathrm{EWG}}e^{i\beta_q^{\mathrm{EWG}}L}\cos\beta_q^{\mathrm{FWG}}L\,\left(1+\frac{U_q}{2}+\frac{1}{2U_q}\right), \tag{24}$$

$$U_q = -i\frac{\mu_0}{\mu_e}\frac{\beta_q^{\mathrm{EWG}}}{\beta_q^{\mathrm{FWG}}}\tan\beta_q^{\mathrm{FWG}}L, \tag{25}$$

$$Y_{qm} = \frac{\kappa_r}{\mu_r}\frac{2}{a}\left[i\left(\frac{\beta_q^{\mathrm{EWG}}}{\beta_q^{\mathrm{FWG}}}\sin\beta_q^{\mathrm{FWG}}L - \frac{\beta_m^{\mathrm{EWG}}}{\beta_m^{\mathrm{FWG}}}\sin\beta_m^{\mathrm{FWG}}L\right)\right.$$
$$\left. + \frac{\mu_0}{\mu_e}\left(\sin\beta_m^{\mathrm{FWG}}L - \sin\beta_q^{\mathrm{FWG}}L\right)\right]e^{i\beta_m^{\mathrm{EWG}}L}I_{qm}, \tag{26}$$

$$Z_{qm} = i\frac{\mu_0}{\mu_e}\left(\frac{\kappa_r}{\mu_r}\frac{2}{a}\right)^2\sum_{s=1}^{N}\frac{\sin\beta_q^{\mathrm{FWG}}L}{\beta_q^{\mathrm{FWG}}}e^{i\beta_m^{\mathrm{EWG}}L}I_{qs}I_{sm}, \tag{27}$$

Note that "I_{mn}" in Eqs. (22) to (27) is defined in Sec. 3. Likewise, the summations in Eqs. (22) and (23) are truncated to N The overall scattering parameters can be calculated by using Eqs. (22) to (27); an example would be demonstrated and discussed in the next section.

5. EXPERIMENTAL SETUP, RESULTS, AND DISCUSSIONS

An experiment was conducted to validate the theory developed in Sec. 4. The standard X-band rectangular waveguide was fabricated by oxygen-free copper and then spitted in half, each of which has identical "L" shape [Fig. 6(a)]. A YIG ferrite [Fig. 6(b)] was chosen as the sample under test, purchased from Pacific Ceramics, Inc. (product #: 39-1780B) with properties prescribed in Sec. 2. The four side walls of the ferrite were plated by copper in order to eliminate the air gaps between sample and waveguide. The ferrite was then enclosed by the two L-shaped waveguide components completely, forming a loaded waveguide [Fig. 6(c)]. This configuration is easy to assemble and disassemble, making this experiment reproducible and repeatable.

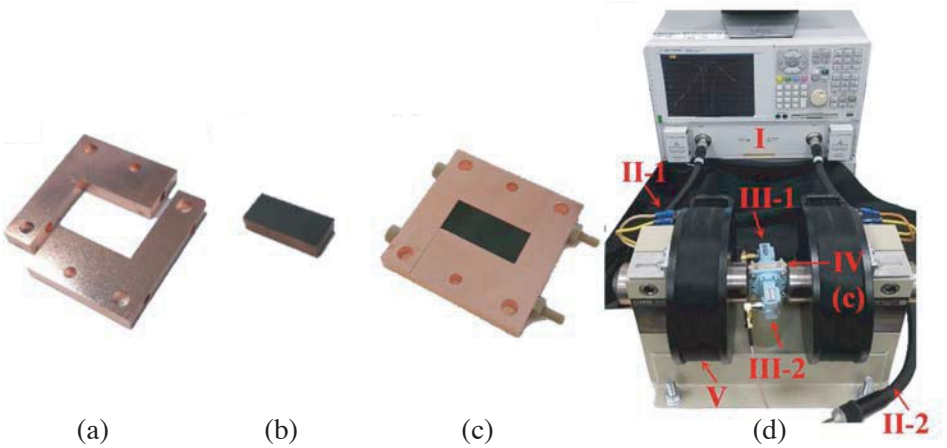

Figure 6. (a) Empty waveguide composed of two L-shaped components. (b) YIG ferrite with cooper coating on its side walls. (c) Ferrite-loaded waveguide system. (d) Overall experimental setup. Part I: performance network analyzer. Part II: flexible coaxial cables. Part III: X-band adapters. Part IV: Ferrite-loaded waveguide system shown in (c). Part V: electromagnet.

A photograph of the overall experimental setup is demonstrated in Fig. 6(d). Part I is the performance network analyzer (PNA, Aglient Technologies E8363B), which was connected with two identical 2.4 mm coaxial cables (parts II-1 and II-2) operated in the coaxial TEM mode. The two cables were connected with two well-calibrated adapters (parts III-1 and III-2) which are able to convert the TEM signal from PNA to $\mathrm{TE}_{10}^{\mathrm{EWG}}$ mode in X-band rectangular waveguide and vice versa. The pre-described ferrite-loaded waveguide was placed in between the two adapters for measurement (part IV). A commercial electromagnet (part V) was used to provide uniform DC magnetic bias. The relation

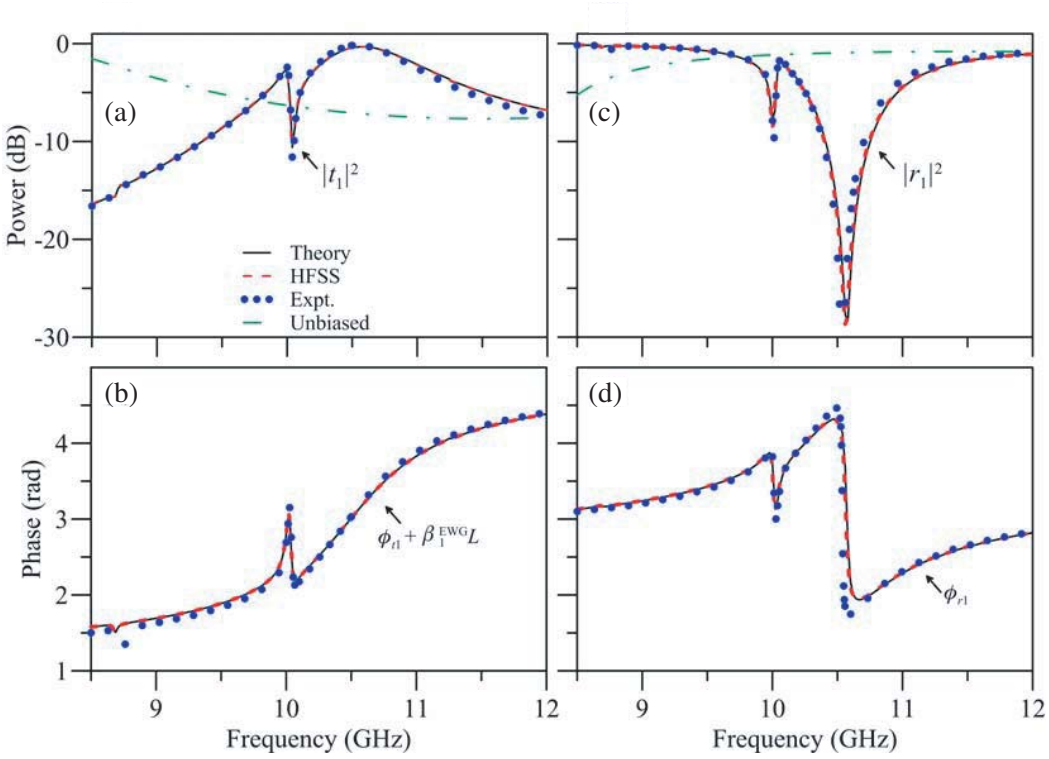

Figure 7. (a) Transmittance $|t_1|^2$. (b) Transmitted phase $\phi_{t1} + \beta_1^{\mathrm{EWG}}L$. (c) Reflectance $|r_1|^2$. (d) Reflected phase ϕ_{r1}. Color codes: black solid curves (theory), red dashed curves (HFSS simulation), and blue circles (experiment). The transmittance and reflectance in the unbiased case are illustrated by the dashed-dotted curves in (a) and (b), respectively.

between the bias and the applied current of electromagnet was pre-tested by a Gauss meter in the absence of sample Then, the electromagnet was adjusted to provide about 1000 Oe under the presence of the ferrite. According to our measurement, the applied DC bias within the ferrite was 1021 ± 30 Gauss with acceptable uniformity. The scattering parameters [$t_1 \equiv |t_1| \exp(i\phi_{t1})$ and $r_1 \equiv |r_1| \exp(i\phi_{r1})$] were then recorded by PNA with 10 averages. The transmittance ($|t_1|^2$) and transmitted phase ($\phi_{t1}+\beta_1^{\mathrm{EWG}}L$) are shown by the blue dots in Figs. 7(a) and 7(b), respectively. The reflectance ($|r_1|^2$) and reflected phase (ϕ_{r1}) are demonstrated by the blue dots in Figs. 7(c) and 7(d), respectively.

On the other hand, Eqs. (22) and (23) with $N = 20$ were used to calculate the theoretical values, which are illustrated in Fig. 7 by the black solid curves. Besides, the transmittance and reflectance in the unbiased case ($H_{\mathrm{DC}} = 0$ and $M_s = 0$) are respectively illustrated in Figs. 7(a) and 7(c) by the green dashed-dotted curves for comparison. The full-wave solver (High-Frequency Structure Simulator, HFSS) was adopted for simulation, which are demonstrated by the red dashed curves in Fig. 7. As shown, three results (experiment, theory, and simulation) have good agreement. It confirms the validity of the present theory and further suggests that our model can be utilized to retrieve all ferrite properties of interest based on the measurable scattering coefficients. Four advantages of such a characterization system are addressed here. Firstly, the allowed bandwidth for measurement is broader than the traditional cavity method [10–13]. Secondly, all the ferrites' electromagnetic physical quantiles, including complex permittivity (ε), saturation magnetization ($4\pi M_s$), and magnetic linewidth (ΔH) can be simultaneously measured in one single compact setup [Fig. 6(d)] without destruction. It could not be achieved by the previous methods [10–13]. Thirdly, since the ferrite under test is fully inserted in a waveguide, the required sample size is minimized to waveguide dimension. It guarantees precise control of sample location and easy-to-achieve uniform magnetic bias. Finally, all components used in measurement can be well calibrated, which is very important for high-precision characterization.

In regard to the results shown in Fig. 7, interesting switching phenomena are observed. In the

presence of bias, a clear constructive-interference peak appears around 10.58 GHz, leading to high transmittance (−0.32 dB) and low reflectance (−28.31 dB). It is referred to an "on state". Such resonant transmission disappears when the bias field is turned off, leading to a relatively low transmittance less than −7 dB (∼ 20%). It is referred to an "off state". The switching behavior results from the fact that the effective permeability (μ_e) of ferrite is strongly suppressed to below 0.6 [Fig. 2(c)], nearly half of 1 when the bias is turned on. Since the round-trip phase changes $\{2\mathrm{Re}[\beta_1^{\mathrm{FWG}}]L$, $\beta_1^{\mathrm{FWG}} = \sqrt{\mu_e\varepsilon\omega^2 - (m\pi/a)^2}\}$ for $\mathrm{TE}_{10}^{\mathrm{FWG}}$ mode propagating inside the biased and the unbiased ferrite have great difference, the multiple-reflection interference conditions change significantly. Besides, we observe very sharp changes of transmittance and reflectance at 10.04 GHz when the bias is applied. This additional resonant peak mainly originates from the modal effect and the multimode interference ($\mathrm{TE}_{10}^{\mathrm{FWG}}$ and $\mathrm{TE}_{20}^{\mathrm{FWG}}$, the only two propagating modes in the ferrite-loaded waveguide), which therefore is not observed in the unbiased case. Similar multimode interference effects have been observed in multimode fibers and high-contrast gratings [31–33]. Through properly controlling the multimode excitation and propagating length, either multimode destructive interference or constructive interference can be achieved, leading to additional stopbands [31, 32] or passbands [31, 32] (like Fano-resonance behavior in the present case around 10.04 GHz), respectively. This interesting feature can be further utilized to design tunable broadband (or narrowband) microwave filters.

6. CONCLUSION

A rectangular waveguide fully loaded with a biased ferrite is proposed to investigate the multimode scattering behaviors of an anisotropic magnetic system. Eigenmode characteristics ($\mathrm{TE}_{m0}^{\mathrm{FWG}}$) in such an anisotropic waveguide are explicitly analyzed. Strong magnetic resonant absorption and stopband effect are observed, which should be carefully avoided in future characterizations or device designs. In addition, the eigenmode electric field profile is invariant in the presence and absence of bias, while the magnetic field profile changes significantly due to the anisotropic permeability tensor of biased ferrite. Based on these eigenmodes' properties, the scattering coefficients for an EM wave (TE_{10} mode) passing through both a single air-ferrite interface and an air-ferrite-air system are analyzed under the consideration of modal effect. The excitation of higher-order modes is demonstrated, and the underlying physics is explained. This work provides an in-depth understanding of ferrite-loaded anisotropic waveguide system, which shows a feasibility for fast and compact ferrite characterization.

ACKNOWLEDGMENT

This work was supported by the National Science Council of the Republic of China, Taiwan, under Grant MOST 107-2112-M-007-015-MY3.

REFERENCES

1. Schloemann, E., "Advances in ferrite microwave materials and devices," *J. Magn. Magn. Mater.*, Vol. 209, No. 1–3, 15–20, Feb. 2000.
2. Capraro, S., J.-P. Chatelon, M. Le Berre, H. Joisten, T. Rouiller, B. Bayard, et al., "Barium ferrite thick films for microwave applications," *J. Magn. Magn. Mater.*, Vol. 272, E1805–E1806, May 2004.
3. Bayard, B., D. Vincent, C. R. Simovski, and G. Noyel, "Electromagnetic study of a ferrite coplanar isolator suitable for integration," *IEEE Trans. Microw. Theory Tech.*, Vol. 51, No. 7, 1809–1814, Jul. 9, 2003.
4. Pardavi-Horvath, M., "Microwave applications of soft ferrites," *J. Magn. Magn. Mater.*, Vol. 215, 171–183, Jun. 2, 2000.
5. Peng, B., H. Xu, H. Li, W. Zhang, Y. Wang, and W. Zhang, "Self-biased microstrip junction circulator based on barium ferrite thin films for monolithic microwave integrated circuits," *IEEE Trans. Magn.*, Vol. 47, No. 6, 1674–1677, Feb. 17, 2011.

6. Darques, M., J. De la Torre Medina, L. Piraux, L. Cagnon, and I. Huynen, "Microwave circulator based on ferromagnetic nanowires in an alumina template," *Nanotechnology*, Vol. 21, No. 14, 145208, Mar. 16, 2010.
7. Ustinov, A., G. Srinivasan, and B. Kalinikos, "Ferrite-ferroelectric hybrid wave phase shifters," *J. Appl. Phys.*, Vol. 90, No. 3, 031913, Jan. 19, 2007.
8. Geiler, A., S. Gillette, Y. Chen, J. Wang, Z. Chen, S. Yoon, et al., "Multiferroic heterostructure fringe field tuning of meander line microstrip ferrite phase shifter," *J. Appl. Phys.*, Vol. 96, No. 5, 053508, Feb. 5, 2010.
9. Morisako, A., T. Naka, K. Ito, A. Takizawa, M. Matsumoto, and Y.-K. Hong, "Properties of Ba-ferrite/AlN double layered films for perpendicular magnetic recording media," *J. Magn. Magn. Mater.*, Vol. 242, 304–310, Apr. 2002.
10. Cohn, S. and K. Kelly, "Microwave measurement of high-dielectric-constant materials," *IEEE Trans. Microw. Theory Tech.*, Vol. 14, No. 9, 406–410, Sep. 1966.
11. Zieba, A. and S. Foner, "Detection coil, sensitivity function, and sample geometry effects for vibrating sample magnetometers," *Rev. Sci. Instrum.*, Vol. 53, No. 9, 1344–1354, Apr. 23, 1982.
12. Krupka, J. and R. G. Geyer, "Complex permeability of demagnetized microwave ferrites near and above gyromagnetic resonance," *IEEE Trans. Magn.*, Vol. 32, No. 3, 1924–1933, May 1996.
13. Green, J. J. and F. Sandy, "A catalog of low power loss parameters and high power thresholds for partially magnetized ferrites," *IEEE Trans. Microw. Theory Tech.*, Vol. 22, No. 6, 645–651, Jun. 1974.
14. Korolev, K. A., L. Subramanian, and M. N. Afsar, "Complex permittivity and permeability of strontium ferrites at millimeter waves," *J. Appl. Phys.*, Vol. 99, No. 8, 08F504, Apr. 21, 2006.
15. Kocharyan, K. N., M. Afsar, and I. I. Tkachov, "Millimeter-wave magnetooptics: New method for characterization of ferrites in the millimeter-wave range," *IEEE Trans. Microw. Theory Tech.*, Vol. 47, No. 12, 2636–2643, Dec. 1999.
16. Ghodgaonkar, D., V. Varadan, and V. Varadan, "Free-space measurement of complex permittivity and complex permeability of magnetic materials at microwave frequencies," *IEEE Trans. Instrum. Meas.*, Vol. 39, No. 2, 387–394, Apr. 1990.
17. Korolev, K. A., S. Chen, and M. N. Afsar, "Complex magnetic permeability and dielectric permittivity of ferrites in millimeter waves," *IEEE Trans. Magn.*, Vol. 44, No. 4, 435–437, Apr. 2008.
18. Catala-Civera, J. M., A. J. Canos, F. L. Penaranda-Foix, and E. de los Reyes Davo, "Accurate determination of the complex permittivity of materials with transmission reflection measurements in partially filled rectangular waveguides," *IEEE Trans. Microw. Theory Tech.*, Vol. 51, No. 1, 16–24, Jan. 2003.
19. Al-Moayed, N. N., M. N. Afsar, U. A. Khan, S. McCooey, and M. Obol, "Nano ferrites microwave complex permeability and permittivity measurements by T/R technique in waveguide," *IEEE Trans. Magn.*, Vol. 44, No. 7, 1768–1772, Jun. 17, 2008.
20. Quéffélec, P., M. Le Floc'h, and P. Gelin, "Nonreciprocal cell for the broadband measurement of tensorial permeability of magnetized ferrites: Direct problem," *IEEE Trans. Microw. Theory Tech.*, Vol. 47, No. 4, 390–397, Apr. 1999.
21. Quéffélec, P., M. Le Floc'h, and P. Gelin, "New method for determining the permeability tensor of magnetized ferrites in a wide frequency range," *IEEE Trans. Microw. Theory Tech.*, Vol. 48, No. 8, 1344–1351, Aug. 2000.
22. O'brien, K. C., "Microwave properties of slabs of uniformly magnetized material filling the cross section of a rectangular waveguide operating in TE_{NO} modes," *IEEE Trans. Microw. Theory Tech.*, Vol. 18, No. 7, 377–382, Jul. 1970.
23. Okubo, K. and M. Tsutsumi, "Waveguide band rejection filter using yttrium iron garnet films," *Electron. Commun. Jpn., Part 2: Electron.*, Vol. 74, No. 5, 40–48, 1991.
24. Tsutsumi, M., H. Shimasaki, and T. Hattori, "Waveguide filters using yttrium iron garnet film," *1992 Asian Pacific Microwave Conference Proceedings*, 183–186, 1992.

25. Ueda, T. and M. Tsutsumi, "Left-handed transmission characteristics of rectangular waveguides periodically loaded with ferrite," *IEEE Trans. Magn.*, Vol. 41, No. 10, 3532–3537, Oct. 2005.
26. Pozar, D. M., *Microwave Engineering*, John Wiley & Sons, 2009.
27. Yao, H.-Y. and T.-H. Chang, "Effect of high-order modes on tunneling characteristics," *Progress In Electromagnetics Research*, Vol. 101, 291–306, 2010.
28. Yao, H.-Y., J.-Y. Jiang, Y.-S. Cheng, Z.-Y. Chen, T.-H. Her, and T.-H. Chang, "Modal analysis and efficient coupling of TE_{01} mode in small-core THz Bragg fibers," *Opt. Express*, Vol. 23, No. 21, 27266–27281, Oct. 2015.
29. Weltner, W., *Magnetic Atoms and Molecules*, Courier Corporation, 1989.
30. Fuller, A. B., *Ferrites at Microwave Frequencies*, IET, 1987.
31. Karagodsky, V. and C. J. Chang-Hasnain, "Physics of near-wavelength high contrast gratings," *Opt. Express*, Vol. 20, No. 10, 10888–10895, 2012.
32. Karagodsky, V., F. G. Sedgwick, and C. J. Chang-Hasnain, "Theoretical analysis of subwavelength high contrast grating reflectors," *Opt. Express*, Vol. 18, No. 16, 16973–16988, 2010.
33. Karagodsky, V., C. Chase, and C. J. Chang-Hasnain, "Matrix Fabry-Perot resonance mechanism in high-contrast gratings," *Opt. Lett.*, Vol. 36, No. 9, 1704–1706, 2011.